Corrosion Science 209 (2022) 110755

Contents lists available at ScienceDirect

Corrosion Science

journal homepage: www.elsevier.com/locate/corsci

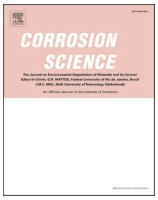

Early-stage evolution of nanoscale oxides on Ni(111) and Ni-Cr (111) surfaces

William H. Blades [a,b], Petra Reinke [a,*]

[a] Department of Materials Science and Engineering, University of Virginia, Charlottesville, VA 22904, USA
[b] Ira A. Fulton Schools of Engineering, Arizona State University, Tempe, AZ 85287, USA

ARTICLE INFO

Keywords:
Mat **A.** (*Ni*)
Mat **A.** (*Ni-Cr*)
Form **B.** (*STM*)
Form **B.** (*STS*)
Prop **C.** (*early-stage oxidation*)
Prop **C.** (*surface science*)

ABSTRACT

The early stages of oxidation on Ni(111) and Ni-18 wt%Cr(111) surfaces were studied with scanning tunneling microscopy/spectroscopy. After exposure to oxygen at 500 °C, chemisorbed p(2 ×2)O adlayers appear on Ni (111) without oxide formation. On the Ni-Cr(111) surface 2D NiO(100) layers rapidly accumulate on the terraces. These coexist with Cr-rich clusters, which coalesce as oxidation progresses. Larger oxide nodules with 3D-island morphology are identified as chromia and are found embedded in the NiO(100). Spectroscopy reveals electronic heterogeneity, highlighting the chemical variation between each oxide species. A schematic is constructed that highlights the associated Ni- and Cr- reaction pathways on Ni-Cr(111) alloy surfaces.

1. Introduction

Oxidation and corrosion initiate at the surface of a material, and unless a protective layer is formed continued material degradation can occur, potentially resulting in enormous economic and environmental costs [1]. The oxidation resistance of metals is often determined by the formation of a protective oxide layer or scale. Ideally, this oxide layer or scale covers the surface and functions as a barrier to alloy degradation. Phenomenological models, such as the Cabrera-Mott model and Wagner's continuum framework have been developed to understand the growth of complete oxide layers at elevated temperatures across different length scales [2–6], and it is well understood that the lateral growth of oxide precipitates is necessary for the formation of a protective layer [7]. However, these models do not capture the oxidation behavior on the surface before a complete layer is formed and describe only internal parabolic growth and transport through a single oxide species. Adaptations to Wagner's theory have identified the conditions necessary for internal/external oxidation and emphasized the importance of an oxide's aspect ratio [8,9].

The significance of oxide morphology was demonstrated recently [10], where the kinetics controlling the oxide island shape and surface morphology were considered through an analogy and variation of Tersoff's thin-film growth model [11]. Modifying these general concepts, a theoretical argument was made that the magnitude of an oxide's Ehrlich-Schwöbel (ES) barrier governs the effective length and general morphology of the initial oxide island, and pathways for manipulating the oxide morphology and nucleation density were discussed [10]. Other recent experimental work also qualitatively adopted thin-film growth concepts to characterize oxide growth modes and morphology evolution [12–16]. These kinetic models provide a path towards a quantitative description of exclusive scale formation at high temperatures, however there still is a significant gap in our understanding of the alloy to oxide transition in the presence of several reactive constituents.

Ni-Cr based superalloys have a high degree of corrosion resistance, which in combination with their mechanical properties, makes their use practical in an array of industrial and military systems [17–20]. The early stages of oxidation on these alloy surfaces is complex, as highlighted by our group's previous STM work on the Ni-Cr(100) surface at temperatures ranging from 300 to 500 °C [15,21,22]. These results revealed rapid growth of NiO(100) across the surface [15,22], and modeling the change in oxide coverage suggested that in this temperature range, oxygen surface diffusion controls the lateral growth of the NiO islands [21]. During this rapid onset of NiO, the Cr-oxide undergoes a much slower lateral propagation, consistent with its known transient growth behavior [23,24]. This begins with the nucleation of small, high density, disk-shaped oxide particles. Continued oxidation of the surface leads to Cr(100) phase segregation, and eventually islands of Cr-oxides with different surface structures are observed laterally growing across the alloy surface [22]. These results emphasize the value of characterizing oxide morphology during early-stage oxidation and the importance

* Corresponding author.
E-mail address: pr6e@virginia.edu (P. Reinke).

https://doi.org/10.1016/j.corsci.2022.110755
Received 25 July 2022; Received in revised form 9 October 2022; Accepted 14 October 2022
Available online 17 October 2022

of understanding atomic-scale oxidation pathways.

The transition from alloy to oxide is sensitive to a wide range of oxidation conditions and material parameters including, but not limited to, surface orientation [25,26], temperature [27,28], and alloy composition [29,30]. The oxidation of Ni(111) accentuates these connections, where the interplay between NiO(100) and NiO(111) growth at different oxidation conditions is particularly interesting [31–37]. Previous studies have shown NiO(100) growth is prominent at intermediate temperatures up to about 230 °C, while at more elevated temperatures and oxygen doses NiO(111) is the more stable orientation [36,37]. The formation of the NiO(100) facet at these intermediate temperatures is favored due to the significantly lower surface energy [38,39] and lattice mismatch at the Ni(111)||NiO(100) interface [36], which contrasts the instability of the NiO(111)-(1 × 1) surface with its large dipole moment [37,39,40]. Oxidation experiments at higher temperatures and larger oxygen doses have shown NiO(111) growth, where the (111) oxide takes a more favorable interfacial relationship with the underlying Ni [37], or forms disordered triangular NiO(111) islands post oxidation [36]. The stability of different NiO surfaces has also been demonstrated during the thermal decomposition of thin layers of NiO(111) and NiO(100), which illustrate a complex interplay between different reconstructions and states of hydroxylation [39]. Moving from Ni(111) to Ni-Cr(111), further changes in oxidation behavior are expected when Cr is alloyed into the matrix, and density functional theory (DFT) studies on Ni-Cr (111) alloys have shown the presence of Cr enhances oxygen absorption [41–45]. Experimental studies on Ni-Cr(111) oxidation are sorely missing and understanding the role of crystallographic orientation on the oxidation process is critical to connect to polycrystalline alloy performance with more complex microstructures.

Our work presented here offers new insight on the early stages of oxidation across a Ni-Cr(111) surface and the competition between Ni and Cr oxide formation. We compare the oxidation of a Ni(111) and Ni-18Cr(111) surface (composition given in wt%) and discuss the morphological changes observed during the early stages of oxidation. We target the early reaction steps for up to 14 L (1 Langmuir=10^{-6} torr s) of oxygen exposure on a Ni-18Cr(111) surface at a substrate temperature of 500 °C and an additional dataset for 40 L of exposure is presented in the Supplementary Material. This temperature was selected to study the competition between Ni and Cr-oxide formation. The qualitative and quantitative analysis of the STM images and scanning tunneling spectra offer a nanoscale view of the process, and are summarized in an oxidation schematic. By examining the early-stage growth of oxides on Ni-Cr surfaces in this pre-Cabrera-Mott regime (the regime prior to the formation of a complete oxide layer), the fundamental phenomena that drive early-stage oxidation can be understood.

2. Methods

Polished MgO(111) single crystals were used as substrates for both the Ni(111) and Ni-Cr(111) thin-film growth. Before deposition, these MgO substrates were prepared using methods outlined in the following publication [46]. Ni (Alfa Aesar 99.999 % purity) and Cr (American Elements, 99.95 % purity) source rods were used, and the deposition took place using a Mantis EV mini e-beam quad-source. This approach yielded 30 nm thin-films with wide terraces and atomically flat surfaces, which STS results show have a characteristic metallic signature (supplementary materials Fig. S2). Prior to deposition, the evaporation rates of Ni and Cr were measured using a quartz crystal monitor (QCM) to accurately adjust the targeted thin-film composition: 0.342 nm min^{-1} for Ni, and 0.072 nm min^{-1} for Cr. The alloy thin-film composition was confirmed ex-situ by energy dispersive spectroscopy (EDS) using a Quanta LV650 SEM with a beam energy of 15 kV. The composition of the film was measured across five different regions on the sample and yielded 17.8 %, 18.7 %, 18.3 %, 17.7 % and 17.2 % (all weight %). Sequential oxidation (steps of +7 L ($p[O_2] = 7 \times 10^{-9}$ mbar, t = 1330 s) of both the Ni(111) and Ni-18Cr(111) thin films took place in our UHV chamber, where oxygen was introduced through a sapphire leak valve while the thin films were held at 500 °C. This temperature was selected to study the competition between Ni and Cr-oxide formation. After each oxidation step, the samples were allowed to cool before the surface evolution was measured with STM and STS. While the Ni(111) and Ni-18Cr(111) samples were deposited a week apart, the same electrochemically etched W-STM tip was used to measure both thin films, and the sequential oxidation steps occurred the same day as each respective thin-film deposition.

The local density of states (LDOS) of the sample surface was measured by taking grid spectra where STS and topography are recorded concurrently. Grid spectra are taken by sweeping the bias voltage (V_{bias}) from ± 3.0 V and measuring an I/V curve for every fourth pixel in the image with an open current-feedback loop, while the topography information was recorded for the next three pixels using a tunneling current (I_t) set at $I_t = 0.1$ nA and a bias voltage $V_{bias} = 3.0$ V. The I/V curves from the grid were numerically differentiated (dI/dV curves) and then normalized by (dI/dV)/(I/V) following the procedure described by Feenstra et al. [47,48]. From these differentiated and normalized curves, the band gap was numerically determined by calculating the region where (dI/dV)/(I/V) is smaller than a threshold value, i.e. where the density of states (DOS) is effectively zero. The (dI/dV)/(I/V) spectra are then spatially resolved by selecting a specific voltage slice (e.g. $V_{slice} = -2.5$ V) to map the variations in the LDOS across the surface. From these data the band gaps, and their associated conduction and valence band values, were also formatted into maps following the procedures outlined in the following reference [49]. Prior to display and analysis of the topography images, each surface was leveled by mean plane subtraction and planarization using the processing software Gwyddion [50]. A MATLAB code implementing routines for gray-scale segmentation was also used to analyze some of the surface features and described in more detail in the following reference [22].

3. Results and discussion

After growth of the Ni(111) and Ni-18Cr(111) thin films, each one was sequentially oxidized at 500 °C, and STM images before and after each oxidation step are shown in Fig. 1. The oxide emerges at a much slower rate on the Ni(111) surface compared to Ni-Cr(111). Indeed, the Ni(111) surface presents a clean metal surface until 14 L when small islands of the Ni(111)-p(2 × 2)O reconstruction are seen, as shown in the inset in Fig. 1(C). A larger version of the inset is included as Supplementary Materials Fig. S1. The reconstruction is not seen on the Ni-Cr film. Areas of unreacted metal are found between the ordered oxygen adlayers, which is consistent with literature [36,37], and no oxide was observed at this temperature and exposure in our experiment. Following the study by Kortan et al [31]. oxygen dissolves in the Ni-bulk and is therefore not available any more to surface oxidation. Their phase diagram for Ni(111) surface reconstructions is in agreement with our observation of Ni(111)-p(2 × 2)O.

The oxide growth across the Ni-18Cr(111) surface resulted in relatively rapid oxide formation after just 7 L of O_2 at 500 °C, Fig. 1(E), which is much faster than on the pure Ni(111) surface shown in Fig. 1 (B). Continuous regions of “smooth” islands of NiO(100) two-dimensional (2D) layers co-exist with oxide particles, which have nucleated across the surface and are quite densely packed. These particles resemble the disk-like Cr-rich oxide particles observed on other low-index Ni-Cr and Cr surfaces [15,22,51],. The effect of additional oxygen exposure on their height and size are discussed later in the manuscript. The shape of the NiO islands and layers is characteristic of the (100) orientation, while NiO(111) islands reported in the literature exhibit a triangular shape imposed by the lattice symmetry [36]. The interpretation of the 2D oxide layers as NiO(100) is addressed in detail later in the manuscript and should be understood here as a preliminary designation.

After an additional + 7 L oxidation (14 cumulative), the NiO(100)

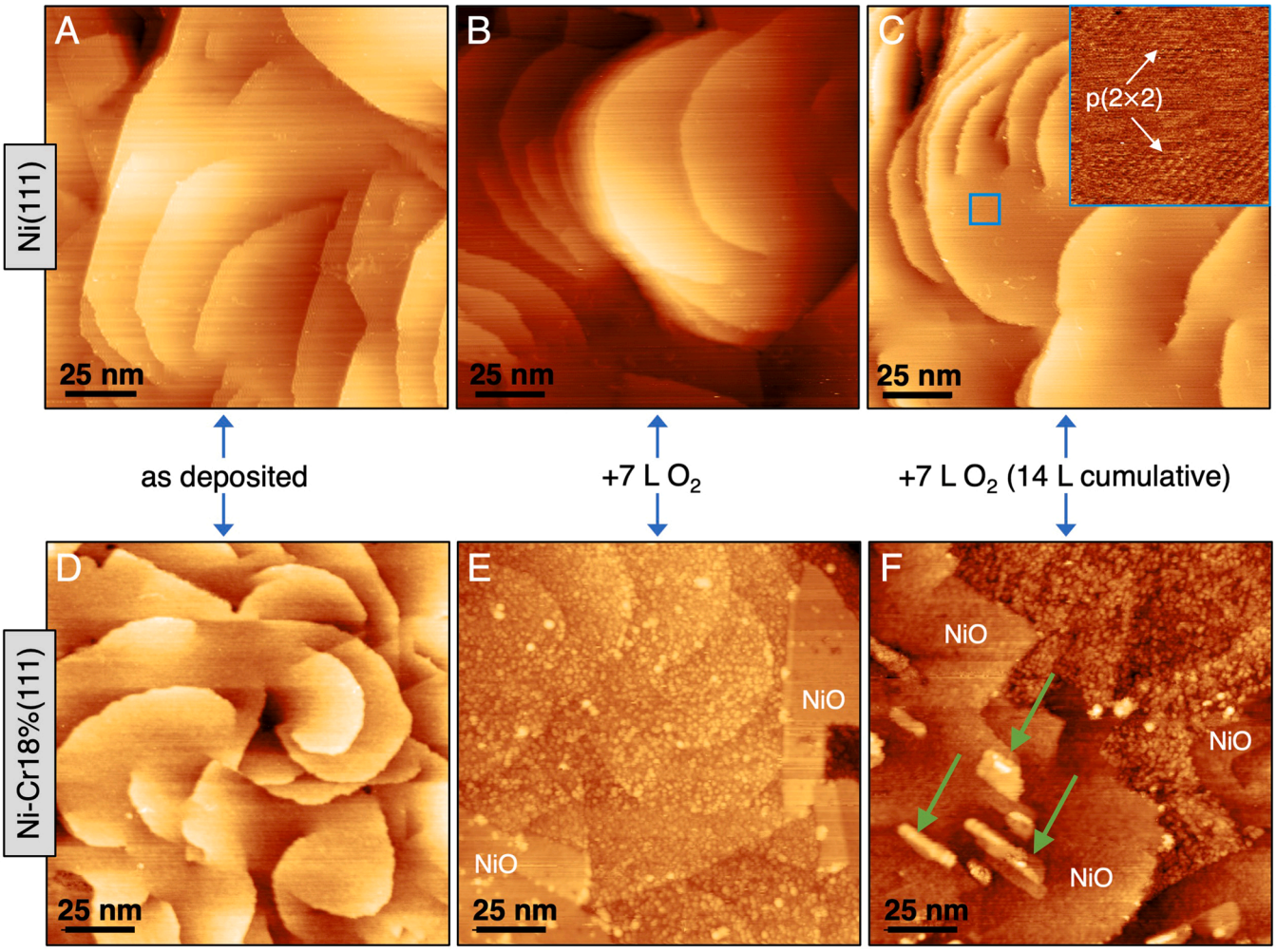

Fig. 1. (A)-(C) STM images of the Ni(111) and (D)-(F) Ni-18 wt%Cr(111) surfaces before and after oxidation at 500 °C. The image inset in (C) highlights the ordered p(2 × 2) adlayer that forms on the Ni(111) surface (10 × 10 nm^2). The green arrows in image (F) mark nodules tentatively assigned to Cr-oxide. **Ni(111):** (A) was measured at $V_{bias} = 0.25$ V and $I_t = 0.5$ nA, (B) $V_{bias} = 2.0$ V and $I_t = 0.1$ nA, (C) at $V_{bias} = -1.0$ V and $I_t = 0.1$ nA. **Ni-Cr18Cr(111):** (D) was measured $V_{bias} = 0.15$ V and $I_t = 0.5$ nA, and (E) and (F) at $V_{bias} = 3.0$ V and $I_t = 0.1$ nA.

coverage has increased, while larger oxide islands or nodules (green arrows) are now visible across the surface and are embedded within the NiO(100) layers, Fig. 1(F). The nature of these features remains subject to discussion, given a lack of atomically resolved structural periodicity, but will be discussed within the context of the available possibilities: NiO, Cr_2O_3 or $NiCr_2O_4$. The NiO presents clearly in the STM images and next-layer NiO maintains its characteristic domains [36] and apparent height [15], so we do not believe these features are the result of multi-layer NiO. $NiCr_2O_4$ spinel island growth has been found on oxidized Ni-Cr surfaces [30] but not at these relatively low cumulative exposures [29]. Our current STM results reveal the apparent height of these oxide features changes significantly as the bias voltage is varied [15], which is consistent with our earlier work supporting the assignment of these nodules as Cr_2O_3 [22]. Indeed, their formation is initiated by high local Cr concentrations at the alloy-oxide interface, but given a clear lack of atomic resolution, we attribute them more generally as a Cr-oxide island or nodule. Our current results reveal that after this oxidation step the regions of large NiO(100) coverage on the terraces tends to coincide with the presence of these oxide nodules. The remaining terraces and step edges are still covered by the smaller Cr-rich oxide particles, which have grown in size.

The oxidation of the Ni-18Cr(111) surface shows in the first oxidation step islands of 2D NiO(100) layers and small oxide particles or disks. These dominant features present differently in the STM images and their size and shape can vary with bias voltage, as shown in Fig. 2. When the alloy-oxide surface is measured at $V_{bias} = -3.0$ V, the oxide particles appear as large protrusions and a near-continuous 2D-oxide layer is bounded by the step edges of the alloy, Fig. 2(A). Once the bias voltage is changed to − 1.0 V the surface appears completely devoid of the oxide particles, and the step edges and terraces of the alloy can be seen clearly, Fig. 2(B). Note that both images, Fig. 2(A) and (B), show the same surface area and were measured consecutively. The Cr-rich oxide clusters and NiO(100) layers are electronically transparent because the bias voltage is attempting to probe states within the band gap of the oxides, which now does not contribute to the tunneling current [52]. In the regions where the NiO(100) 2D layers are present, some step edges are faceted (white arrows in B), which is comparable to the formation of NiO (100) on Ni-Cr(100), albeit without the emergence of a low-index grain boundary across the step edge [15]. In contrast, the NiO(100) islands are pinned by the alloy step edges. The image inset in Fig. 2(B) shows periodic rows across the 2D NiO(100) layers, which present most prominently when measured at relatively low positive bias voltages from 0.1 to 1 V.

A high resolution STM image of the NiO(100) 2D layer can be seen in Fig. 3(A), where periodic rows extend across the surface, some interrupted by additional larger periodic features. Line scans taken across the surface highlight the variation in periodicity and are provided adjacent to the STM image in Fig. 3(B)-(D). Arrows corresponding to the line scan

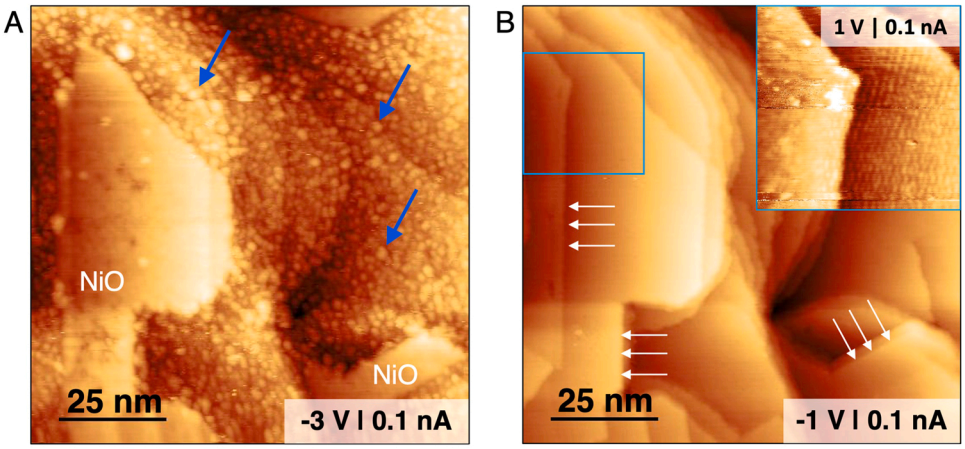

Fig. 2. STM topography images of the identical section on the Ni-18 wt%Cr(111) surface after 7 L of exposure. Image (A) was measured at $V_{bias} = -3.0$ V and $I_t = 0.1$ nA, while image (B) was taken at $V_{bias} = -1.0$ V and $I_t = 0.1$ nA within the band gap of the oxide islands and clusters. The variation in bias voltage affects which oxides islands and clusters are visible on the surface. At the lower bias voltages, the surface appears smooth. An image of the empty states, measured at $V_{bias} = 1.0$ V and $I_t = 0.1$ nA, is provided in the 25 × 25 nm^2 image inset in (B) and small periodic rows can be seen. The white arrows point out faceted step edges.

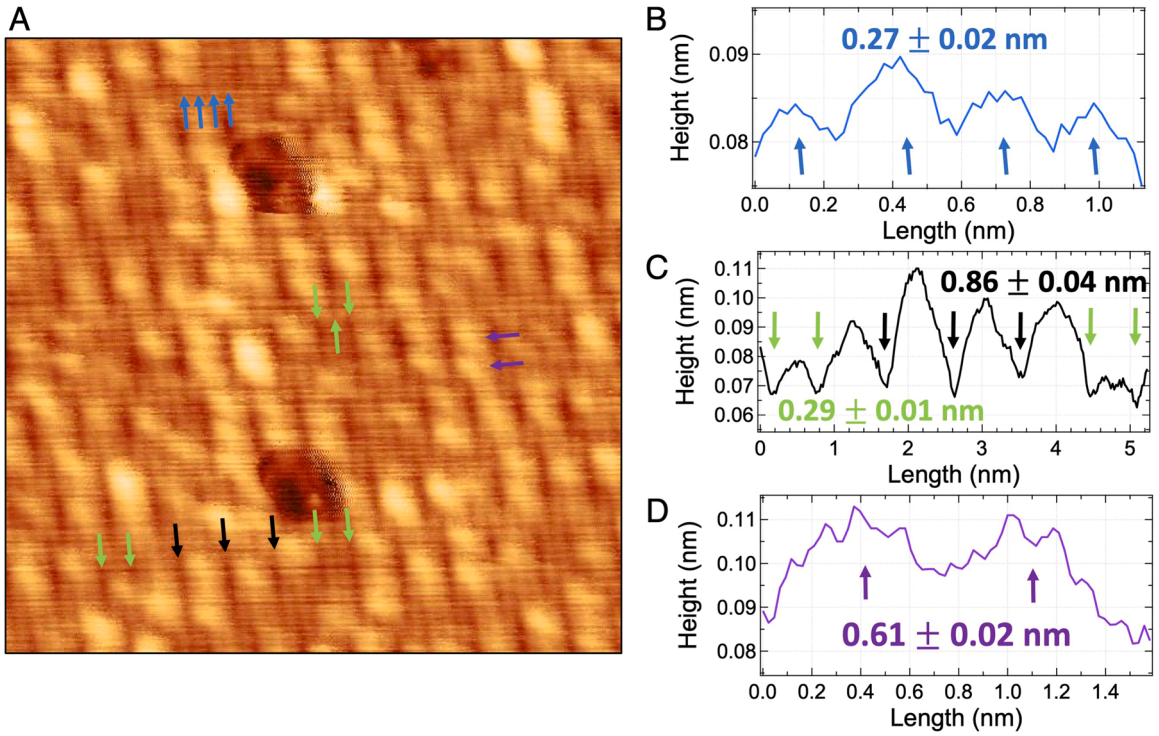

Fig. 3. High resolution image of the NiO-Ni(111) interface. (A) The topography image is 12 × 12 nm^2 and was taken at $V_{bias} = 0.1$ V and $I_t = 0.5$ nA. The colored arrows superimposed over the image accompany the line scans in (B)-(D), which guide the readers eye to the various periodic domains found on the Ni-Cr(111) surface after oxidation. Detailed models of the corresponding surface structures are given in [36].

positions are overlaid on the image. The smallest periodic spacing, indicated by blue and green arrows, is about 0.27 ± 0.02 nm, while the larger spacing marked by the purple and black arrows spans 0.61 ± 0.02 nm and 0.86 ± 0.04 nm, respectively. These periodicities match well with the atomic spacing of the NiO(100) structure and its local (2 × 2), (2 × 3) and (3 × 3) NiO(100)-Ni(111) domains identified and described in detail in the literature [36,39]. Such a structure allows the NiO(100) layer to sit on top of the (111) alloy surface, with a small lattice mismatch, as every third Ni (or O) atom along ⟨110⟩ is located in a threefold hollow site across the underlying Ni-Cr(111) surface. The interpretation of the NiO layers as being of the (100) orientation is therefore supported by the island shape and the high resolution images.

Our results show the Cr-oxidation pathway presents different morphologies and growth initiates with the nucleation of small oxide particles. While these particles lack a clear structural periodicity, they have been measured on a variety of different low-index Ni-Cr and Cr surfaces [15,22,51], and Monte Carlo simulations have provided evidence they are likely connected to Cr clustering on the Ni-Cr alloy surface [22]. A quantitative assessment of these Cr-rich oxide particles as a function of oxygen exposure is given in Fig. 4. Our STM results show these features present differently after the 7 L and 14 L O_2 cumulative exposures, Fig. 4 (A)-(B), and line scans are provided to highlight these changes, Fig. 4 (C)-(D). Taking numerous STM topography images with identical imaging conditions, the change in apparent height and lateral area was determined and summarized in Fig. 4(E)-(F). Note that due to the convolution of all STM images with the tip shape, the lateral dimensions of small clusters are overestimated and the "oxide area" is not an absolute value but should be interpreted in comparison between the two oxidation steps. After the first 7 L oxidation step at 500 °C, the Cr-rich

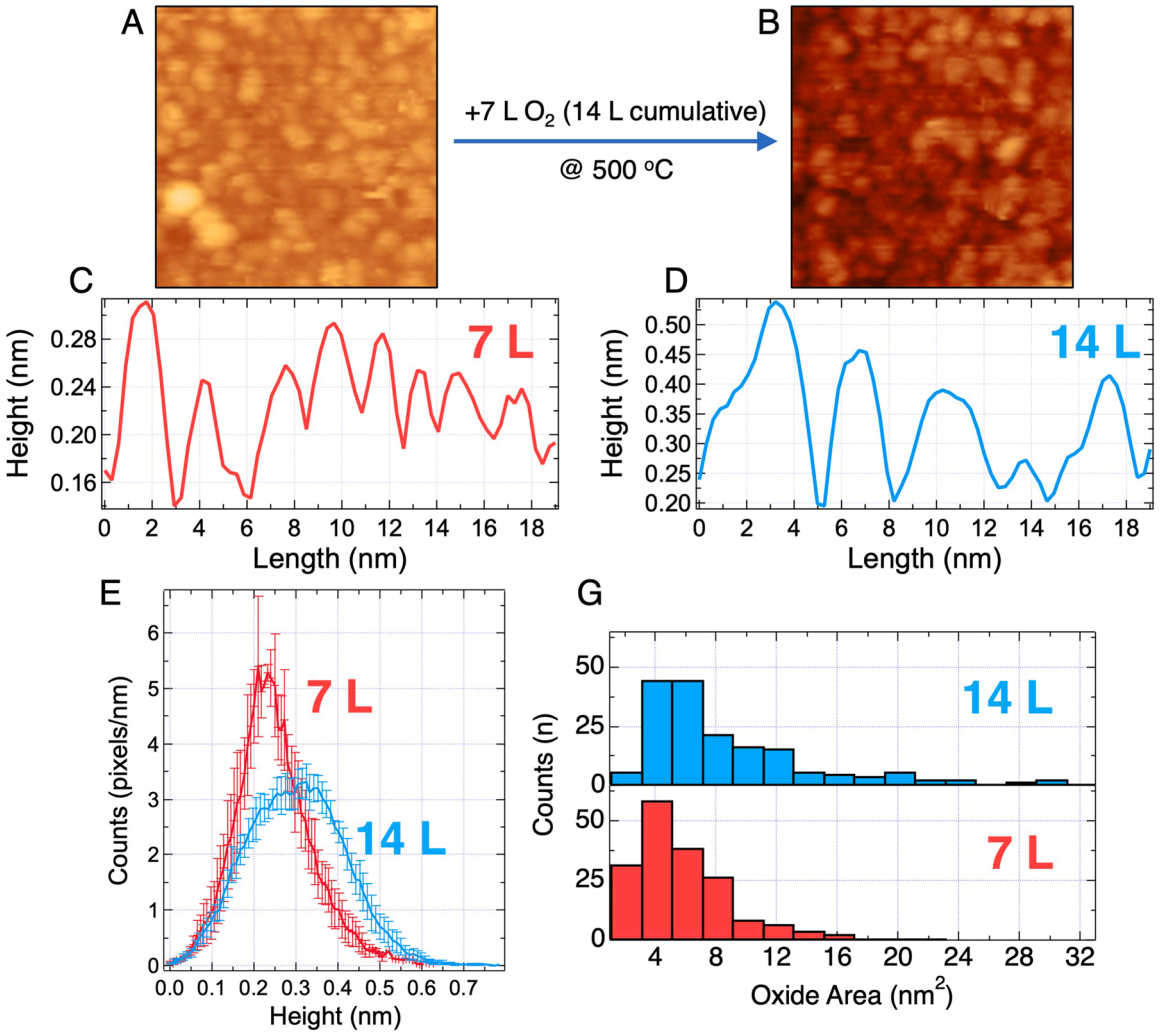

Fig. 4. Comparison of the smaller Cr-rich oxide particles after the 7 L and 14 L exposures. The STM images after 7 L (A) and 14 L (B) and accompanying line scans (C) and (D). The height (E) and area (G) distributions of these particles are summarized. The data were obtained from 25 × 25–32 × 32 nm^2 areas, cropped from lager images and all measured with identical imaging conditions. Each image was flattened and a polynomial background along the x-direction was removed to correct for any raster streaking along the x-direction. Images (A) and (B) are 25 × 25 nm^2 and measured with V_{bias} = 3.0 V, I_t = 0.1 nA.

particles have a maximum apparent height centered at 0.21 nm, and an average area of 4.99 ± 0.26 nm^2. An additional + 7 L of oxidation (14 cumulative) and the particle's maximum apparent height increases slightly to 0.33 nm, while their lateral area swells to an average of 8.42 ± 0.50 nm^2. Cr-rich oxide particles of similar shape and size are found on Ni-Cr(100) [22], which after undergoing ripening and coalescence, seed the formation of a continuous chromia layer. These results demonstrate that the early growth steps of the passive chromia layer initiates with the formation of these particles and lack the strong interfacial ordering seen for NiO-Ni interfaces. However unlike on the (100) NiCr surface, these particles are still found on the surface after 14 L. Furthermore, the additional oxygen exposure is accompanied by the appearance of large Cr-oxide nodules already mentioned in the presentation of Fig. 1(F).

From the STM results, after a cumulative oxidation of 14 L three distinct oxide features are present, the NiO(100), Cr-rich oxide particles and larger oxide nodules. The electronic structure of the surface was measured with STS to gain more insight into these oxide features. A 3 × 3 STS grid spectrum was taken with a voltage range of ± 3.0 V over a 200 × 200 nm^2 area, and the results were processed into DOS and band gap maps, Fig. 5. A blue dashed box in the topography image in Fig. 5(A) outlines the spatial region matching the DOS and band gap maps, Fig. 5 (B)-(C). Specific regions within these oxide features are selected and the STS curves within that region are averaged (60–120 curves) for a better signal to noise ratio, Fig. 5(D).

The NiO(100) layers in region (1) are electronically homogeneous across most of this area, and only small variations in band gap can be seen near the edges of the Cr-rich oxide particles, which are best visible in the band gap and DOS maps. The smaller Cr-oxide particles have a relatively large band gap and there is some tentative evidence that the gap scales with the height of the particle (supplementary materials Fig. S1). Nonetheless, patches of the alloy surface with a metallic signature (2) can be seen in between these smaller Cr-rich oxide particles. This signature suggests the Ni-Cr(111) surface becomes locally depleted in oxygen for the benefit of Cr-oxidation, and is in agreement with our previous work highlighting an oxygen capture radius of less than a nanometer exists around a growing oxide particle perimeter [21]. Region (3) corresponds to the oxide nodules, where the average (dI/dV)/(I/V) curves show the valence band is suppressed and cannot be effectively measured due to insufficient conductivity within the oxide nodule. The lack of conductivity in the valence band, whether due to the oxide thickness or a wide band gap, is a consequence of a low number of states available for tunneling [53].

A schematic for the general oxidation behavior of a Ni-Cr(111) surface is provided in Fig. 6, and the result of an additional oxidation step for 40 L(cumulative) is included in the supplementary materials Fig. S4.

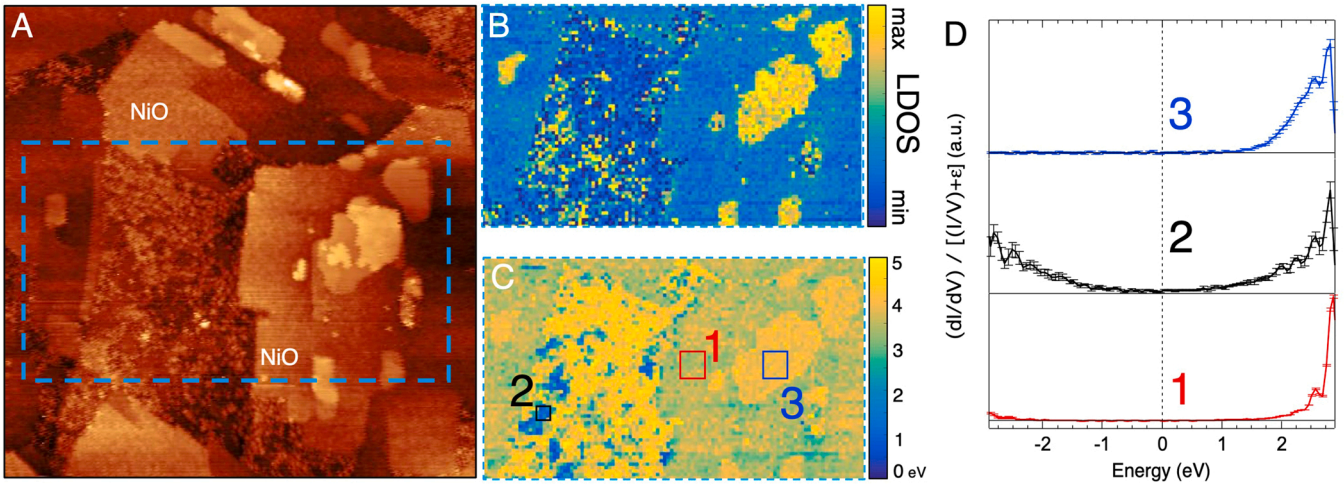

Fig. 5. STS measurements of the Ni-18Cr surface after a cumulative 14 L. The STS data were taken from the blue-dashed square, marked in the topography image, and formatted into an LDOS map (B) at V_{slice}= 2.4 eV, see method section for explanation, and a band gap map (C). The averaged STS curves (30–60 curves) in (D) are marked with squares in (C) and provide details about the NiO(100) (1), patches of Ni-Cr alloy (2), and nodules tentatively assigned to Cr-oxide (3). The STM topography was measured at V_{bias} = 3.0 V and I_t = 0.1 nA and is 200 × 200 nm^2. Values above 4 eV in the band gap map indicate an oxide layer which is too thick to provide a full spectrum, and the tunneling current from the filled states becomes zero as seen in spectrum (3) panel (D).

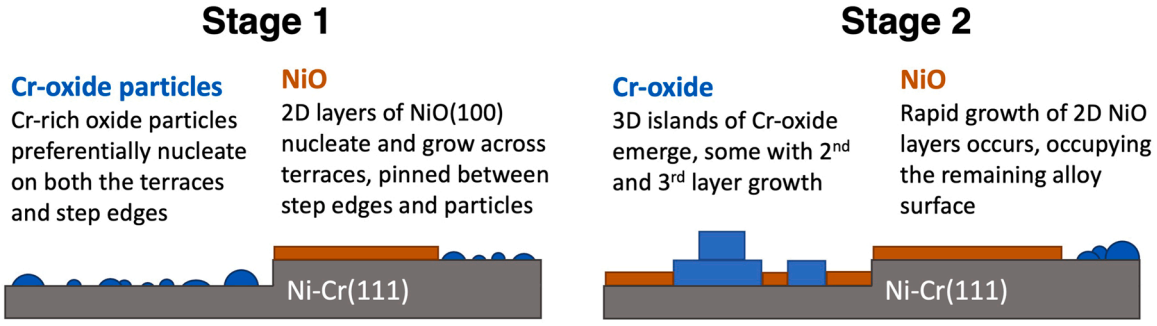

Fig. 6. A visual schematic for the oxidation of Ni-Cr(111) surfaces, capturing both Ni and Cr oxidation pathways.

Given the distinctive manner in which each oxide phase developed across the surface, the oxidation pathways of the Ni and Cr can be organized in 2 stages. The oxidation step observed after the 7 L exposure (stage 1) begins with the 2D-layer growth of NiO(100) across the Ni-Cr (111) terraces. This behavior is interesting because previous literature has reported that NiO(111) growth should begin on Ni(111) at the temperature used in our work but is suppressed on the alloy surface [37, 52]. Hildebrandt et al. provided reasoned epitaxial arguments for NiO (100) formation, where the instability of the unreconstructed NiO(111) octupole surface and lower lattice strain at the NiO(100)-(111) interface are responsible for the growth of this preferential facet [36]. While these arguments do not entirely explain the difference in thermal stability of NiO(100) versus NiO(111), our results show the addition of Cr has accelerated the onset of NiO(100) growth across the surface, which is likely a consequence of Cr locally enhancing oxygen bonding [41,42, 44]. These trends in alloy reactivity are commensurate with a shift in the D-band center as Sprowl et al. reported [45].

Our results show that the Ni-Cr(111) surface indeed prefers the formation of islands of 2D NiO(100) layers. After growth begins, the interfacial stability and rapid growth of the NiO(100) layer precludes thermal decomposition of the oxide film, meaning the attachment rate of atoms at the NiO(100) growth front exceeds their detachment rate. In the early stages of NiO(100) growth the formation of a layer is favored, adopting a Frank-van der Merwe (layer by layer) growth mode, and no NiO(111) islands are observed [10]. The coverage, respectively number of layers at this point of the oxidation experiment, is insufficient to ascertain step-flow growth. Recent experimental studies on poly-crystalline alloys [29] show that NiO overgrows the Cr-oxide formed early in the oxidation process. However, we cannot confirm that this process is already fully developed at the exposures studied here. The NiO (100) regions are typically pinned between the alloy step edges and areas saturated with Cr-rich oxide particles, while for Ni-Cr(100)||NiO (100) the oxide restructures the step edges. The distinct differences between the Ni-Cr(100)||NiO(100) and Ni-Cr(111)||NiO(100) interfaces are the cause of these variations in morphology.

As oxygen exposure increases (Fig. 6, Stage 2), the Cr-rich oxide particles begin to coalesce and new (presumably) Cr-oxide nodules, islands with a distinct 3D growth mode, are observed on the surface. Supplementary Fig. S4 shows the next step of oxidation for an exposure of 40 L, which leads to a highly complex morphology. These features remain difficult to assess with STM and are included therefore in the supplementary material. At this stage of the Cr-oxidation pathway, second- and third-layer Cr-oxide growth is preferential to continued lateral propagation and a Vollmer-Weber growth mode develops. In general, the stability of the Ni-Cr(111)-NiO(100) interface promotes the Frank-van der Merwe growth for NiO(100), while Cr-oxide and chromia do not wet the alloy surface and form clusters and 3D nodules. We propose that these inherent differences between the competing oxides and their interaction with the alloy surfaces is critical to their performance in the protective layer, and the variability in oxide growth behavior as a function of crystallographic orientation adds an additional constraint on predicting oxide functionality in theoretical models.

Future work will have to connect nanoscale mechanisms of oxidation to macroscopic performance of the protective layer.

4. Conclusions

The sequential in situ oxidation of Ni(111) and Ni-18Cr(111) thin films at 500 °C has been studied with STM and STS. The STM images before and after each oxidation step have highlighted the effect of crystallography and Cr addition on the oxidation pathways of these surfaces early in the oxidation process. The Ni(111) surface was found to saturate with oxide at a much slower rate compared to the Ni-Cr(111) surface. Ni(111) remains mostly metallic during oxygen exposure and islands of Ni(111)-p(2 × 2)O adlayers are observed. The oxidation of the Ni-18Cr(111) alloy thin film shows two distinct oxide features after just 7 L of O_2. Islands of 2D NiO(100) layers formed on the terraces, which contrasts previous reports that NiO(111) islands should begin to emerge at these temperatures [37,39]. Small Cr-rich oxide particles nucleate across terraces and alloy steps while the NiO(100) oxide layers are confined to individual alloy terraces. After an additional + 7 L oxidation (14 cumulative) the growth of 3D nodules, similar to those found on Ni-Cr(100) surfaces after comparable exposures, commences [15,22]. The nodules which are embedded in the NiO(100) layers are tentatively assigned to chromia. The Cr-oxide particles, which densely populate the entire surface in between NiO layers, increase in size with continued oxygen exposure which is consistent with a ripening process. We assume that the surface is not stationary – once oxygen is absorbed the local composition of the alloy will change in response to the modulation of the local chemical potential. Hence the assumption of a random solid solution and homogeneous element distribution in the surface will break down and lead to the formation of distinct Ni-oxide and Cr-oxide regions. These results support the significant role of crystallography and interface registry on the oxidation pathways of low-index Ni-Cr surfaces.

CRediT authorship contribution statement

W.H.B. wrote the manuscript and analyzed the data. **P.R.** conceived and guided the study, and co-wrote the manuscript. All authors contributed to the interpretation of the work, edited the manuscript and approved the final version.

Declaration of Competing Interest

The authors declare that they have no known competing financial interests or personal relationships that could have appeared to influence the work reported in this paper.

Data availability

The experimental data from this report will be made available if a reasonable request is made to the corresponding author.

Acknowledgements

W.H.B. and P.R. would like to thank the Office of Naval Research for supporting the MURI Program entitled “Corrosion in 4D,” Grant N00014-14-1-0675, under program manager Dr. David Shifler. P.R. acknowledges the support from the National Science Foundation (NSF) (Award No. DMR-2004326) by the Division of Materials Research—Metals and Metallic Nanostructures. W.H.B would also like to acknowledge support from the Office of Naval Research, Multidisciplinary University Research Initiative program, “From Percolation to Passivation (P2P): Multiscale Prediction and Interrogation of Surface and Oxidation Phenomena in Multi-Principal Element Alloys” under Grant Number N00014-20-1-2368.

Appendix A. Supporting information

Supplementary data associated with this article can be found in the online version at doi:10.1016/j.corsci.2022.110755.

References

[1] B.A. Shaw, R. Kelly, What is corrosion? Electrochem. Soc. Interface 15 (2006) 24–26.
[2] A. Atkinson, Transport processes during the growth of oxide films at elevated temperature, Rev. Mod. Phys. 57 (1985) 437–470, https://doi.org/10.1103/RevModPhys.57.437.
[3] C. Wagner, Equations for transport in solid oxides and sulfides of transition metals, Prog. Solid State Chem. 10 (1975) 3–16, https://doi.org/10.1016/0079-6786(75)90002-3.
[4] N. Cabrera, N.F. Mott, Theory of the oxidation of metals, Rep. Prog. Phys. 12 (1949) 163, https://doi.org/10.1088/0034-4885/12/1/308.
[5] A. Seyeux, V. Maurice, P. Marcus, Oxide film growth kinetics on metals and alloys I. Physical model, J. Electrochem. Soc. 160 (2013) C189–C196, https://doi.org/10.1149/2.036306jes.
[6] M.H.R. Lankhorst, H.J.M. Bouwmeester, H. Verweij, Thermodynamics and transport of ionic and electronic defects in crystalline oxides, J. Am. Ceram. Soc. 80 (1997) 2175–2198, https://doi.org/10.1111/j.1151-2916.1997.tb03107.x.
[7] R.A. Rapp, Kinetics, microstructures and mechanism of internal oxidation - its effect and prevention in high temperature alloy oxidation, Corrosion 21 (1965) 382–401, https://doi.org/10.5006/0010-9312-21.12.382.
[8] J.-B. Leblond, A note on a nonlinear version of Wagner’s Classical Model of internal oxidation, Oxid. Met. 75 (2011) 93–101, https://doi.org/10.1007/s11085-010-9222-6.
[9] J.-B. Leblond, M. Pignol, D. Huin, Predicting the transition from internal to external oxidation of alloys using an extended Wagner model, C. R. Mécanique 341 (2013) 314–322, https://doi.org/10.1016/j.crme.2013.01.003.
[10] W.H. Blades, E.J. Opilia, K. Sieradzki, Mechanisms of exclusive scale formation in the high temperature oxidation of alloys, J. Electrochem. Soc. 169 (2022), 061501, https://doi.org/10.1149/1945-7111/ac751f.
[11] J. Tersoff, A.W. Denier van der Gon, R.M. Tromp, Critical island size for layer-by-layer growth, Phys. Rev. Lett. 72 (1994) 266–269, https://doi.org/10.1103/PhysRevLett.72.266.
[12] G. Zhou, L. Luo, L. Li, J. Ciston, E.A. Stach, J.C. Yang, Step-edge-induced oxide growth during the oxidation of Cu surfaces, Phys. Rev. Lett. 109 (2012), 235502, https://doi.org/10.1103/PhysRevLett.109.235502.
[13] G. Zhou, L. Luo, L. Li, J. Ciston, E.A. Stach, W.A. Saidi, J.C. Yang, In situ atomic-scale visualization of oxide islanding during oxidation of Cu surfaces, Chem. Commun. 49 (2013) 10862–10864, https://doi.org/10.1039/C3CC46684A.
[14] L. Luo, L. Zou, D.K. Schreiber, M.J. Olszta, D.R. Baer, S.M. Bruemmer, G. Zhou, C.-M. Wang, In situ atomic scale visualization of surface kinetics driven dynamics of oxide growth on a Ni–Cr surface, Chem. Commun. 52 (2016) 3300–3303, https://doi.org/10.1039/C5CC09165A.
[15] W.H. Blades, P. Reinke, From alloy to oxide: capturing the early stages of oxidation on Ni–Cr(100) alloys, ACS Appl. Mater. Interfaces 10 (2018) 43219–43229, https://doi.org/10.1021/acsami.8b15210.
[16] X.-X. Yu, M.A. Taylor, J.H. Perepezko, L.D. Marks, Competition between thermodynamics, kinetics and growth mode in the early-stage oxidation of an equimolar CoCrFeNi alloy, Acta Mater. 196 (2020) 651–659, https://doi.org/10.1016/j.actamat.2020.06.056.
[17] J.H. Perepezko, The hotter the engine, the better, Science 326 (2009) 1068–1069, https://doi.org/10.1126/science.1179327.
[18] J.-L. Strudel, Mechanical properties of multiphase alloys, in: R.W. Cahn, P. Haasen† (Eds.), Phys. Metall., fourth ed., Oxford, North-Holland, 1996, pp. 2105–2206, https://doi.org/10.1016/B978-044489875-3/50030-2.
[19] A.P. Mouritz, Superalloys for gas turbine engines, in: Introd. Aerosp. Mater., Woodhead Publishing, 2012, pp. 251–267, https://doi.org/10.1533/9780857095152.251.
[20] K. Horke, A. Meyer, R.F. Singer, Metal injection molding (MIM) of nickel-base superalloys, in: D.F. Heaney (Ed.), Handb. Met. Inject. Molding, second ed., Woodhead Publishing, 2019, pp. 575–608, https://doi.org/10.1016/B978-0-08-102152-1.00028-3.
[21] R. Ramanathan, G. Ramalingam, J.H. Perepezko, P. Reinke, P.W. Voorhees, Evolution of NiO island size distributions during the oxidation of a Ni–5Cr alloy: experiment and modeling, ACS Appl. Mater. Interfaces 10 (2018) 9136–9146, https://doi.org/10.1021/acsami.7b18539.
[22] W.H. Blades, M.R. Barone, P. Reinke, Initial atomic-scale oxidation pathways on a Ni–15Cr(100) alloy surface, Npj Mater. Degrad. 5 (2021) 1–10, https://doi.org/10.1038/s41529-021-00164-7.
[23] B. Chattopadhyay, G.C. Wood, The transient oxidation of Fe-Cr and Ni-Cr alloys, J. Electrochem. Soc. 117 (1970) 1163, https://doi.org/10.1149/1.2407761.
[24] G.C. Wood, B. Chattopadhyay, Transient oxidation of Ni-base alloys, Corros. Sci. 10 (1970) 471–480, https://doi.org/10.1016/S0010-938X(70)80032-4.
[25] K. Gusieva, K.L. Cwalina, W.H. Blades, G. Ramalingam, J.H. Perepezko, P. Reinke, J.R. Scully, Repassivation behavior of individual grain facets on dilute Ni–Cr and Ni–Cr–Mo alloys in acidified chloride solution, J. Phys. Chem. C 122 (2018) 19499–19513, https://doi.org/10.1021/acs.jpcc.8b04306.

[26] P.R. Norton, R.L. Tapping, J.W. Goodale, A photoemission study of the interaction of Ni(100), (110) and (111) surfaces with oxygen, Surf. Sci. 65 (1977) 13–36, https://doi.org/10.1016/0039-6028(77)90289-8.
[27] Y. Xie, J. Zhang, D.J. Young, Effect of temperature on oxidation behaviour of Ni-Cr alloys in CO_2 atmosphere, ECS Trans. 75 (2017) 19, https://doi.org/10.1149/07528.0019ecst.
[28] X. Zhang, D.W. Shoesmith, Influence of temperature on passive film properties on Ni–Cr–Mo Alloy C-2000, Corros. Sci. 76 (2013) 424–431, https://doi.org/10.1016/j.corsci.2013.07.016.
[29] C. Volders, V.A. Angelici, I. Waluyo, A. Hunt, L. Árnadóttir, P. Reinke, Unraveling the role of tungsten as a minor alloying element in the oxidation NiCr alloys, Npj Mater. Degrad. 6 (2022) 1–11, https://doi.org/10.1038/s41529-022-00265-x.
[30] L. Luo, L. Zou, D.K. Schreiber, D.R. Baer, S.M. Bruemmer, G. Zhou, C.-M. Wang, In-situ transmission electron microscopy study of surface oxidation for Ni–10Cr and Ni–20Cr alloys, Scr. Mater. 114 (2016) 129–132, https://doi.org/10.1016/j.scriptamat.2015.11.031.
[31] A.R. Kortan, R.L. Park, Phase diagram of oxygen chemisorbed on nickel (111), Phys. Rev. B 23 (1981) 6340–6347, https://doi.org/10.1103/PhysRevB.23.6340.
[32] T. Okazawa, T. Nishizawa, T. Nishimura, Y. Kido, Oxidation kinetics for Ni(111) and the structure of the oxide layers, Phys. Rev. B 75 (2007), 033413, https://doi.org/10.1103/PhysRevB.75.033413.
[33] G.T. Tyuliev, K.L. Kostov, XPS/HREELS study of NiO films grown on Ni(111), Phys. Rev. B. 60 (1999) 2900–2907, https://doi.org/10.1103/PhysRevB.60.2900.
[34] H. Conrad, G. Ertl, J. Küppers, E.E. Latta, A LEED/UPS study on the interaction of oxygen with a Ni(111) surface, Solid State Commun. 17 (1975) 497–500, https://doi.org/10.1016/0038-1098(75)90486-X.
[35] T.M. Christensen, C. Raoul, J.M. Blakely, Change in oxide epitaxy on Ni(111): Effects of oxidation temperature, Appl. Surf. Sci. 26 (1986) 408–417, https://doi.org/10.1016/0169-4332(86)90114-5.
[36] S. Hildebrandt, Ch Hagendorf, T. Doege, Ch Jeckstiess, R. Kulla, H. Neddermeyer, Th Uttich, Real time scanning tunneling microscopy study of the initial stages of oxidation of Ni(111) between 400 and 470 K, J. Vac. Sci. Technol. A 18 (2000) 1010–1015, https://doi.org/10.1116/1.582292.
[37] J.I. Flege, A. Meyer, J. Falta, E.E. Krasovskii, Self-limited oxide formation in Ni (111) oxidation, Phys. Rev. B 84 (2011), 115441, https://doi.org/10.1103/PhysRevB.84.115441.
[38] D. Wolf, Reconstruction of NaCl surfaces from a dipolar solution to the Madelung problem, Phys. Rev. Lett. 68 (1992) 3315–3318, https://doi.org/10.1103/PhysRevLett.68.3315.
[39] N. Kitakatsu, V. Maurice, P. Marcus, Local decomposition of NiO ultra-thin films formed on Ni(111, Surf. Sci. 411 (1998) 215–230, https://doi.org/10.1016/S0039-6028(98)00372-0.
[40] P.W. Tasker, The stability of ionic crystal surfaces, J. Phys. C Solid State Phys. 12 (1979) 4977–4984, https://doi.org/10.1088/0022-3719/12/22/036.
[41] N.K. Das, T. Shoji, Early stage oxidation of Ni–Cr binary alloy (111), (110) and (100) surfaces: a combined density functional and quantum chemical molecular dynamics study, Corros. Sci. 73 (2013) 18–31, https://doi.org/10.1016/j.corsci.2013.03.020.
[42] A.J. Samin, C.D. Taylor, First-principles investigation of surface properties and adsorption of oxygen on Ni-22Cr and the role of molybdenum, Corros. Sci. 134 (2018) 103–111, https://doi.org/10.1016/j.corsci.2018.02.017.
[43] V. Alexandrov, M.L. Sushko, D.K. Schreiber, S.M. Bruemmer, K.M. Rosso, Adsorption and diffusion of atomic oxygen and sulfur at pristine and doped Ni surfaces with implications for stress corrosion cracking, Corros. Sci. 113 (2016) 26–30, https://doi.org/10.1016/j.corsci.2016.10.001.
[44] N.K. Das, T. Shoji, Adsorption and diffusion of H and O on an Ni(111) surface containing different amounts of Cr, Appl. Surf. Sci. 445 (2018) 217–228, https://doi.org/10.1016/j.apsusc.2018.03.134.
[45] L.H. Sprowl, B.M. Adam, J.D. Tucker, L. Árnadóttir, First-principles study of the products of CO_2 dissociation on nickel-based alloys: trends in energetics with alloying element, Surf. Sci. 677 (2018) 219–231, https://doi.org/10.1016/j.susc.2018.06.011.
[46] G. Ramalingam, P. Reinke, Growth of Ni and Ni-Cr alloy thin films on MgO(001): effect of alloy composition on surface morphology, J. Appl. Phys. 120 (2016), 225302, https://doi.org/10.1063/1.4971261.
[47] R.M. Feenstra, Tunneling spectroscopy of the (110) surface of direct-gap III-V semiconductors, Phys. Rev. B 50 (1994) 4561–4570, https://doi.org/10.1103/PhysRevB.50.4561.
[48] R.M. Feenstra, J.A. Stroscio, A.P. Fein, Tunneling spectroscopy of the Si(111)2 × 1 surface, Surf. Sci. 181 (1987) 295–306, https://doi.org/10.1016/0039-6028(87)90170-1.
[49] W.H. Blades, N.J. Frady, P.M. Litwin, S.J. McDonnell, P. Reinke, Thermally induced defects on WSe2, J. Phys. Chem. C 124 (2020) 15337–15346, https://doi.org/10.1021/acs.jpcc.0c04440.
[50] D. Nečas, P. Klapetek, Gwyddion: an open-source software for SPM data analysis, Open Phys. 10 (2011) 181–188, https://doi.org/10.2478/s11534-011-0096-2.
[51] V. Maurice, S. Cadot, P. Marcus, XPS, LEED and STM study of thin oxide films formed on Cr(110, Surf. Sci. 458 (2000) 195–215, https://doi.org/10.1016/S0039-6028(00)00439-8.
[52] V. Maurice, G. Despert, S. Zanna, M.-P. Bacos, P. Marcus, Self-assembling of atomic vacancies at an oxide/intermetallic alloy interface, Nat. Mater. 3 (2004) 687–691, https://doi.org/10.1038/nmat1203.
[53] Ch Sommerhalter, Th.W. Matthes, J. Boneberg, P. Leiderer, M.Ch Lux-Steiner, Tunneling spectroscopy on semiconductors with a low surface state density, J. Vac. Sci. Technol. B Microelectron. Nanometer Struct. Process. Meas. Phenom. 15 (1997) 1876–1883, https://doi.org/10.1116/1.589571.